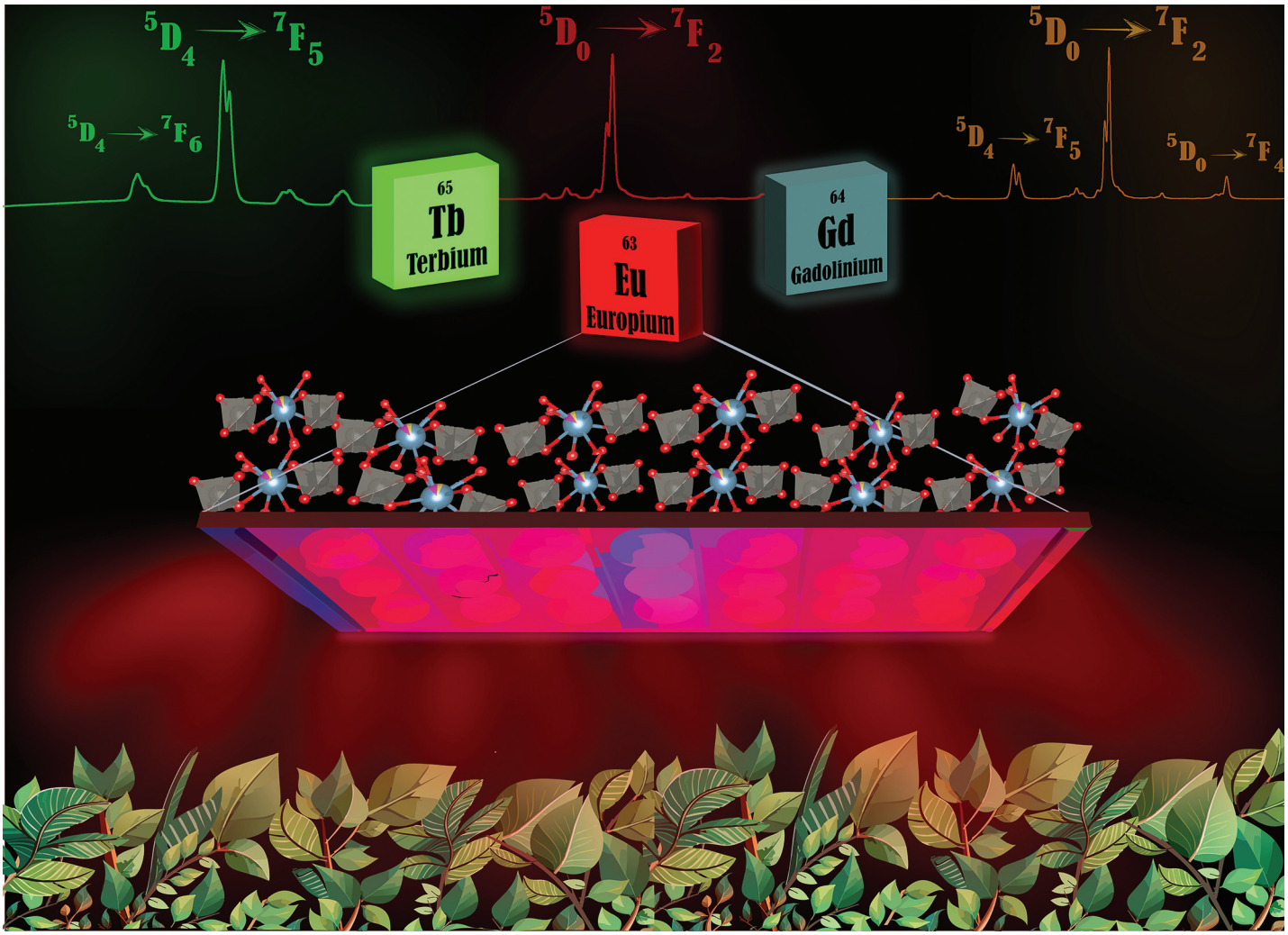

Showcasing research from Professor Gomez group, Faculty of Chemistry, University of San Luis, San Luis, Argentina.

Lanthanide-dependent photoluminescence and thin film fabrication of host $CaWO_4$ micro-materials for potential indoor plant growth applications

A set of $CaWO_4$ micro materials doped with lanthanide ions (Tb, Gd and Eu) exhibit promising visible photoluminescence for a range of growing plants.

Image reproduced by permission of Vanesa Ponce, Carlos A. López and Germán E. Gomez from *Dalton Trans.*, 2025, **54**, 7252.

As featured in:

See Carlos A. López, Germán E. Gomez *et al.*, *Dalton Trans.*, 2025, **54**, 7252.

ROYAL SOCIETY OF CHEMISTRY

rsc.li/dalton

Registered charity number: 207890

Dalton Transactions

ROYAL SOCIETY OF CHEMISTRY

PAPER

View Article Online
View Journal | View Issue

Cite this: *Dalton Trans.*, 2025, **54**, 7252

Lanthanide-dependent photoluminescence and thin film fabrication of host $CaWO_4$ micro-materials for potential indoor plant growth applications†

Vanesa Ponce,[a,b] Rik Van Deun,[c] Liliana P. Fernández,[d] Griselda E. Narda,[a,b] Carlos A. López *[a,b] and Germán E. Gomez *[a,b]

Received 14th February 2025,
Accepted 26th March 2025

DOI: 10.1039/d5dt00366k

rsc.li/dalton

A set of scheelite ($CaWO_4$, **CWO**) doped samples with formula $Ca_{1-2x}Ln_xNa_xWO_4$ (x = 0 and 0.1; Ln = Eu, Tb and Gd) (**Eu@CWO**, **Tb@CWO** and **Gd@CWO**) and doped phases with combinations $Ln_xLn'_y$ = $Eu_{0.05}Tb_{0.05}$, $Eu_{0.05}Gd_{0.05}$, $Tb_{0.05}Gd_{0.05}$ (**Eu,Tb@CWO**, **Eu,Gd@CWO** and **Tb,Gd@CWO**) and $Eu_{0.033}Tb_{0.033}Gd_{0.033}$ (**Eu,Tb,Gd@CWO**) were prepared by a modified four-step sol–gel method followed by calcination at mild temperatures. The solids were characterized by X-ray powder diffraction (XRPD) and scanning electron microscopy (SEM). An in-depth analysis of the structure and the impact of the synthesis approach on crystallite shape and size was carried out using Rietveld refinements. Besides, the solid-state photoluminescence was studied in terms of excitation, emission 4f–4f* transitions, lifetimes (τ_{obs}), radiative and non-radiative constants (k_r and k_{nrad}), energy transfer migration analysis and europium quantum yields. Finally, the Eu-containing CWO samples were selected as a potential emitter device constructed using a spin-coating technique giving rise to homogeneous coatings onto square glass substrates. These results are promising for the design and construction of devices based on wolframate micro-sized materials with emission properties and potential applications in plant cultivation LEDs, sensing, photocatalysis and solar cells.

Introduction

Indoor plant cultivation, a relevant method for plant growth, has been attracting increasing attention, since it can be independent of inclement weather events such as drought, storm, fog, flood, *etc*.[1] Also, it is well known that light can affect the growth process of plants. Blue (410–500 nm), red (600–690 nm) and far-red (700–740 nm) light wavelengths are critical for the phototropism, photomorphogenesis and photosynthesis processes in plants, respectively.[2,3] Currently, solid-state light-emitting diodes (LEDs) have emerged as one of the most effective lighting options for agricultural applications due to their numerous advantages. These include a wide variety of spectral types that align well with key spectral ranges essential for photosynthesis and photomorphogenesis. LEDs also enable the generation of specific single-color light or complex spectra, ensuring uniform distribution of targeted wavelengths on crops.[4,5] In addition to these benefits, they offer high efficiency, energy savings, environmental sustainability, long lifespan, and compact design.[6–9] Among them, phosphor-converted LEDs stand out as promising choices for achieving highly efficient lighting solutions for indoor agricultural environments.

Previous studies have identified two types of phytochromes: one is the red-light-absorbing form (P_r), with a maximum absorption peak at 670 nm, which remains physiologically inactive; the other is the far-red-light-absorbing form (P_{fr}), with a peak at 730 nm, which is biologically active.[10–13] These two forms can interconvert when exposed to their respective wavelengths. The balance between red and far-red light influences the plant's transition from vegetative to floral growth. Therefore, adjusting this ratio effectively regulates plant development based on its specific needs for red and far-red light.

[a]*Instituto de Investigaciones en Tecnología Química (INTEQUI-CONICET), Almirante Brown 1455, 5700 San Luis, Argentina*
[b]*Universidad Nacional de San Luis, Ejército de los Andes, 950 (5700), San Luis, Argentina. E-mail: germangomez1986@gmail.com*
[c]*L^3 – Luminescent Lanthanide Lab, f-element coordination chemistry, Ghent University, Department of Chemistry, Krijgslaan 281, Building S3, 9000 Gent, Belgium*
[d]*Instituto de Química San Luis (INQUISAL), Universidad Nacional de San Luis, CONICET, Ejército de los Andes, 950 (5700) San Luis, Argentina*

†Electronic supplementary information (ESI) available: Tables of Rietveld analysis, 4f–4f* transition assignments, decay profiles and fittings, host-matrix emission spectra and extra SEM micrographs. See DOI: https://doi.org/10.1039/d5dt00366k

Trivalent lanthanide ions are used as special building blocks for the development of optical materials with a variety of applications due to specific features such as pure colour emission accompanied by fine 4f–4f transitions, long lifetime values and tuneable optical responses over a variable wavelength range including the UV, visible and infrared regions. The mentioned properties make lanthanides attractive for constructing optical devices, sensors, lasers, up-converters, and light displays.[14–20] Lanthanide ions gradually fill the 4f orbitals from $4f^0$ to $4f^{14}$ (La^{3+} to Lu^{3+}). Besides, the electronic configurations $[Xe]f^n$ (n = 0–14) generate a plethora of electronic energy levels,[21] resulting in unique optical features.[22] With the exception of La^{3+} and Lu^{3+}, the remaining Ln^{3+} ions exhibit emission signals in the ultraviolet (UV) to visible and near-infrared (NIR) regions. It is well known that Sm^{3+}, Eu^{3+}, Tb^{3+}, Dy^{3+} and Tm^{3+} ions can emit orange, red, green, yellow and blue light, respectively. Other ions such as Nd^{3+}, Yb^{3+} and Er^{3+} display near-infrared luminescence. Also, rational combinations of lanthanide ions can achieve interesting optical properties due to energy transfer pathways in up-conversion and down-conversion mechanisms.[6]

Moreover, metal wolframate-based derivatives, such as polyoxometalates (POMs)[23] and scheelite structural type ($CaWO_4$) compounds,[24–26] have been proposed as efficient host matrixes for lanthanide ions. The reason for selecting wolframate (with general formula AWO_4 (A: Ca/Ba/Sr)) as a host is because d-block and f-block transition elements have an advantage over other host lattices due to the presence of a broad excitation band in the UV region.[27] This band is attributed to the O–W charge transfer. Furthermore, it is well known that the $CaWO_4$ phosphor presents diverse optical applications in scintillators, light-emitting diodes (LEDs), solid state lasers and fluorescent lamps.[28] Some reports have demonstrated the NIR emission of $CaWO_4$ doped with $Gd^{3+}/Er^{3+}/Yb^{3+}$ or Er^{3+}/Yb^{3+} as up-converting materials.[29,30] Besides, $CaWO_4$ has been employed as an efficient matrix for Eu^{3+} by controlling doping through different synthetic approaches.[31]

In spite of many investigations regarding the structure and optical properties of $CaBO_4$:Eu^{3+} (B = Mo, W) microparticles and nanoparticles, there are very few reports focusing on an in-depth study of photophysical parameters such as luminescence lifetime (τ_{obs}), radiative (k_r) and non-radiative (k_{nrad}) constants and quantum yield parameters, which are important properties to be evaluated for designing new luminescent materials. Previously, we reported two nano-sized luminescent $Ca_{0.8}Ln_{0.1}Na_{0.1}WO_4$ (Ln = Eu^{3+}, Sm^{3+}) samples synthesized using a three-step methodology including two mechanochemical treatments followed by calcination.[32] The nano-sized solids resulted in visible emitters of orange and red light under UV excitation, respectively. The Eu^{3+}-doped sample exhibited a hypersensitive transition ($^5D_0 \rightarrow {}^7F_2$), which was selected as a robust signal for a chemical sensor towards cations in aqueous media. Moreover, some authors relate the impact of the synthesis methodology onto the crystalline sizes and shapes, and their further applications.[33–36]

In this work, we report the synthesis using a sol–gel method and overall characterization of doped-lanthanide $CaWO_4$ compounds. An in-depth structural and microstructural analysis was carried out by employing powder X-ray diffraction accompanied by Rietveld refinements. Such an in-depth study has not been commonly reported for scheelite samples, which makes this one important for the design of micro-materials and nano-materials. Also, the solid-state photoluminescence (SSPL) was analysed by recording the excitation and emission spectra and calculating the τ_{obs} value from the decay profiles. Besides, the europium quantum yields, radiative and non-radiative constants, and CIE colour coordinates were calculated and related to the energy transfer processes between lanthanides and the host matrix. Finally, a thin film was fabricated using a spin-coating method, by controlling several experimental parameters to yield a homogeneous coating on a glass substrate. These results are a contribution to luminescence devices based on luminescent lanthanide micro-materials.

Experimental

Synthesis

Powder samples with stoichiometries $Ca_{1-2x}Ln_xNa_xWO_4$ (x = 0 and 0.1; Ln = Eu, Tb and Gd) and co-doped phases with $Ln_xLn'_y$ = $Eu_{0.05}Tb_{0.05}$, $Eu_{0.05}Gd_{0.05}$, $Tb_{0.05}Gd_{0.05}$ and $Eu_{0.033}Tb_{0.033}Gd_{0.033}$ were prepared using a modified sol–gel Pechini method[37] in four steps. Stoichiometric quantities of $Ca(NO_3)_2{\cdot}4H_2O$, anhydrous Na_2CO_3, $(NH_4)_6H_2W_{12}O_{40}{\cdot}xH_2O$, $Eu(NO_3)_3{\cdot}5H_2O$, $Tb(NO_3)_3{\cdot}5H_2O$, $Gd(NO_3)_3{\cdot}6H_2O$ and citric acid were mixed in 50 mL of distilled water in a beaker under constant stirring and heated at 110 °C. When gel formation was observed, the mixture was removed from the hot plate. Then, the covered beaker was placed in a furnace for 5 h at 180 °C until the formation of a porous and spongy brown "soufflé". Once dried, the "soufflé" was manually ground with an agate mortar. After that, the samples were calcined to 500 °C for 10 h. A scheme of the synthesis is shown in Fig. 1.

Eu@CWO, **Eu,Tb@CWO**, **Eu,Gd@CWO** and **Eu,Tb,Gd@CWO** were selected for thin film preparation by employing spin-coating apparatus (Laurell model WS-650-23-B). First, the powdered samples were ground with an agate mortar for 1 h and then 50 mg of material was added to 1 mL of a toluene–tetrahydrofuran (1 : 1.85 ratio) solution of 2% polymethyl methacrylate (PMMA). After that, the suspension was sonicated for 1 h. For the deposition, glass substrates of 1.3 cm × 1.3 cm that had been previously cleaned with ethanol were used. Besides, to improve the thin film quality, multiple variables were modified during the deposition such as sonication time, revolutions per minute (rpm), step time, concentration and drop volume of the added suspension.

Powder X-ray diffraction (PXRD)

The solid phase identification and characterization was carried out by PXRD using a Rigaku Ultima IV diffractometer with CuKα (λ = 1.5418 Å) radiation. The patterns were refined with the Rietveld method using the FullProf program.[38,39] The

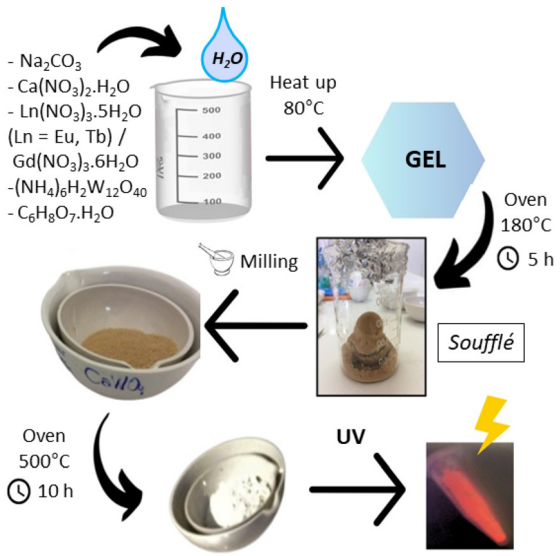

Fig. 1 Scheme of synthesis of **Ln@CWO** compounds.

profile shape was modelled using the Thompson–Cox–Hastings pseudo-Voigt function,[40] and the instrumental resolution parameters were considered in the refinements to obtain the microstructural parameters. The parameters *U*, *V*, and *W* are fixed and correspond to the instrumental broadening; hence, only the Lorentzian isotropic strain (*X*) and size (*Y*) were refined. From these parameters, the apparent size and strain were calculated from the Scherrer and Stokes–Wilson formulas, respectively.

Scanning electron microscopy (SEM)

SEM micrographs were obtained and energy dispersive analysis during X-ray spectroscopy (EDS) was conducted on FEI Quanta 200 equipment. Samples were placed on an adhesive carbon tape coated with gold prior to analysis.

Photoluminescence spectra and lifetime measurements

The steady-state and time-resolved luminescence measurements were performed on an Edinburgh Instruments FLSP920 spectrometer setup, using a 450 W xenon lamp as the steady-state excitation source and a 60 W pulsed xenon lamp as the time-resolved excitation source (operating at a pulse frequency of 100 Hz). The emission was detected using a Hamamatsu R928P PMT photomultiplier tube for the visible range. Excitation spectra were corrected for the xenon lamp emission profile, whereas emission spectra were corrected for the detector response curve. All measurements were carried out at a step size of 0.1 nm. Time-resolved measurements were performed using a Continuum® Surelite I laser (450 mJ@1064 nm), operating at a repetition rate of 10 Hz and using the third harmonic (355 nm) as the excitation source. Commission Internationale de l'Eclairage (CIE) (*x*,*y*) colour coordinates were calculated using the MATLAB program.

Results and discussion

From the synthetic approach, powdered samples were obtained. The morphology of the particles was studied using SEM techniques to analyse the impact of the synthesis on the resulting size and shape of the particles. From the SEM analysis, aggregates of around 10–200 μm and some flat structures with a cross-section of 15 μm for **Eu@CWO** were observed (see Fig. 2). Similar particles were observed for **Tb@CWO** and **Eu, Tb@CWO** as shown in Fig. S1 and S2 (ESI†). In addition, the chemical composition was verified from EDS as illustrated in Fig. S3† for these phases. These insights highlight the influence of the synthesis methodology on the resulting particle shape and size. In our previous contribution, the $Ca_{0.8}Ln_{0.1}Na_{0.1}WO_4$ phase (Ln^{3+} = Sm and Eu) was obtained as rounded nanoparticles using the grinding method.[32]

Crystal structure

Initial identification and crystal refinements of all samples were achieved using PXRD data. All doped samples were indexed to the scheelite structure ($CaWO_4$) in the tetragonal space group $I4_1/a$ (#88)[41] and no impurities were observed. As

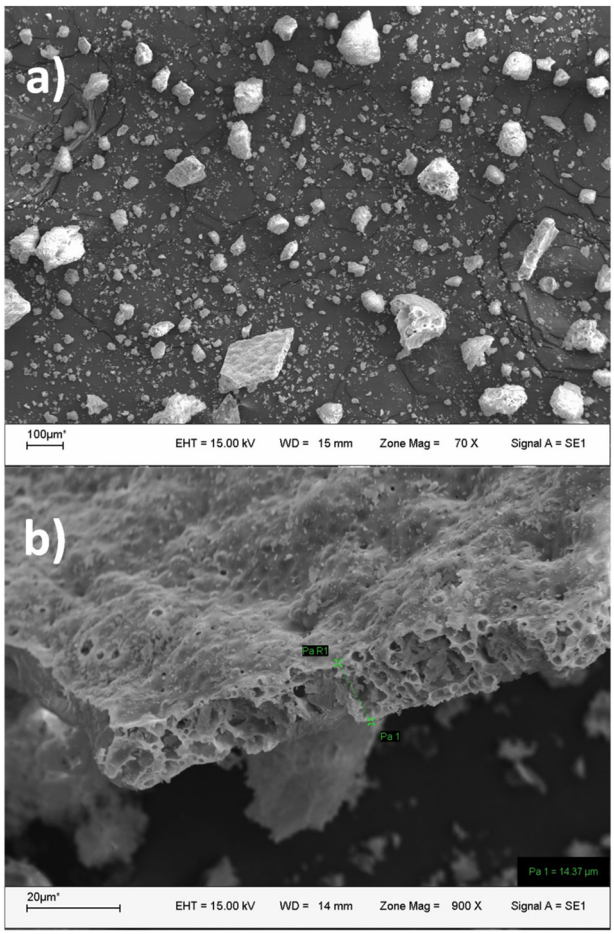

Fig. 2 SEM images of **Eu@CWO** particles at (a) 70× and (b) 900× magnification.

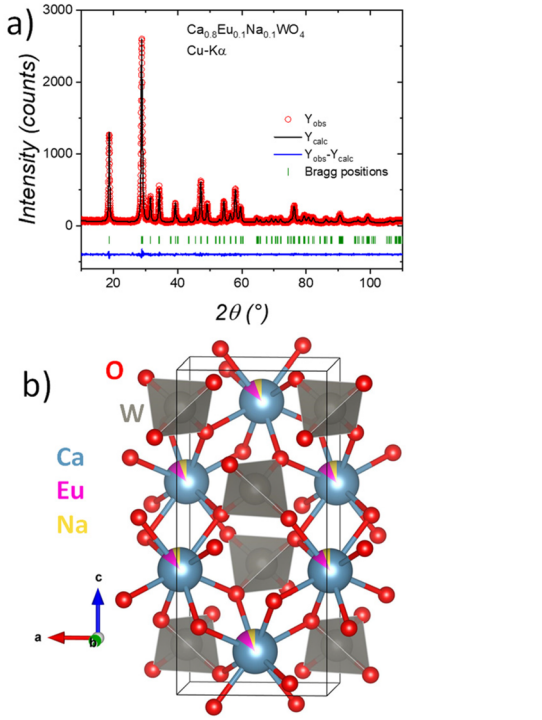

Fig. 3 (a) Observed (red points), calculated (black full line) and difference (bottom) Rietveld profiles for **Eu@CWO** at room temperature. (b) Schematic view of the crystal structure of **Eu@CWO**.

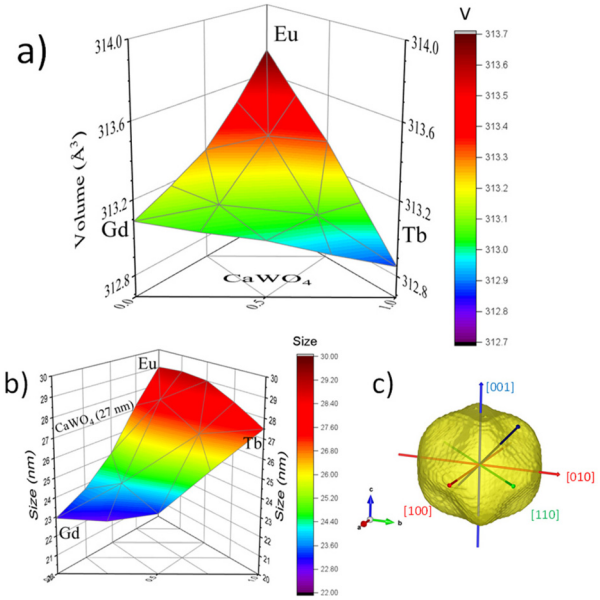

Fig. 4 (a) Unit-cell volume for different doped phases. The unit-cell volume for the pristine phase is 312.68(1) Å^3. (b) Crystallite size for different doped phases. The crystallite size for the pristine phase is 27 nm. (c) Crystallite shape obtained for $CaWO_4$ from SPH formalism.

is well known, in the scheelite structure, W forms tungstate units (WO_4) with a tetrahedral geometry, while Ca^{2+} is coordinated by eight oxygen atoms. This last site is co-doped with $Ln_{0.1}Na_{0.1}$, which was confirmed from occupancy factor refinement. All samples present a crystallographic stoichiometry close to $Ca_{0.8}Ln_{0.1}Na_{0.1}WO_4$. The Rietveld refinement plot for **Eu@CWO** as a representative of the family of micromaterials is shown in Fig. 3a, while the Rietveld refinements for the remaining pristine **CWO** and doped phases are illustrated in Fig. S4.† The main crystallographic results for selected phases are listed in Table 1, and the remaining phase parameters are listed in Table S1.† Fig. 3b shows a schematic view of the crystal structure of **Eu@CWO**.

The structural impact of Ln^{3+}/Na^+ co-doping on the unit-cell volume is plotted in Fig. 4a as a 3D ternary graph. As can be seen, the doped phases present a higher volume than the pristine phase (312.68 Å^3) in agreement with the variation between Ca^{2+} and Ln^{3+}/Na^+ ionic radii ($r_{Ca^{2+}}$ = 1.12 Å, r_{Na^+} = 1.18 Å, $r_{Eu^{3+}}$ = 1.07 Å, $r_{Gd^{3+}}$ = 1.05 Å and $r_{Tb^{3+}}$ = 1.04 Å).[42] In

Table 1 Main crystallographic parameters of crystalline samples of $CaWO_4$ and Ln/Na-doped phases with Ln = Eu, Gd and Tb

ABO_4	Ca	$Ca_{0.8}Eu_{0.1}Na_{0.1}$	$Ca_{0.8}Gd_{0.1}Na_{0.1}$	$Ca_{0.8}Tb_{0.1}Na_{0.1}$
a (Å)	5.2427(1)	5.2497(2)	5.2461(2)	5.2464(2)
c (Å)	11.3764(3)	11.3841(5)	11.3761(5)	11.3720(5)
V (Å^3)	312.68(1)	313.74(2)	313.09(2)	313.01(2)
A (8d) 0,1/4,5/8				
Occ (Ca/Ln)	1	0.828(4)/0.084(4)	0.764(4)/0.116(4)	0.832(4)/0.084(5)
U^{iso} (Å^2)	0.010(1)	0.010(2)	0.013(2)	0.008(2)
W (8c) 0,1/4,1/8				
Occ	1	1	1	1
U^{iso} (Å^2)	0.0080(4)	0.0093(5)	0.0093(6)	0.0099(5)
O (16f) x,y,z				
X	0.754(1)	0.762(2)	0.761(2)	0.765(2)
Y	0.400(1)	0.398(2)	0.398(2)	0.400(2)
Z	0.0414(6)	0.041(1)	0.041(1)	0.040(1)
U^{iso} (Å^2)	0.018(3)	0.021(4)	0.018(4)	0.023(4)
Occ	1	1	1	1
Reliability factors				
R_p, R_{wp}, χ^2, R_{Bragg}	5.5%, 7.8%, 0.6, 1.3%	5.3%, 7.2%, 0.5, 1.2%	5.3%, 7.2%, 0.6, 1.2%	5.3%, 7.2%, 0.6, 1.3%

addition, the increases in ionic size, from Tb^{3+} to Eu^{3+}, included in the phases with two and three lanthanides, are observed in terms of the volume variations as revealed in the ternary graph (see Fig. 4a).

On the other hand, the diffraction peaks in all patterns present non-negligible broadening consistent with reduced crystallite sizes. Initial refinements were made considering isotropic size and strain effects yielding a proper fit in all phases; however, closer inspection reveals that several lines are not properly modelled showing a line of anisotropic broadening. This suggested that using a model of crystallite size (or strain) can enhance the pattern fitting; thus, after several tests the use of anisotropic crystallite size with spherical harmonics (SPH) treatment leads to a considerable improvement in the fitting. In the refinement of the SPH formalism, eight additional parameters were fitted according to the $4/m$ Laue class. Fig. S5† compares the results of the refinements using both isotropic and anisotropic models for the Eu^{3+}-doped phase as representative of the series.

The main microstructural results, apparent size and strain, are listed in Table S2.† The average size is plotted in Fig. 4b where the effect after Ln^{3+}/Na^{+} doping can be observed, while the phases doped with Gd^{3+} present lower average sizes than the other phases (Eu^{3+}, Tb^{3+} and Eu^{3+}/Tb^{3+}) with respect to the pristine phase, which present a larger size. The size anisotropy was obtained for each sample, and that for $CaWO_4$ is shown in Fig. 4c. For this pristine phase, the crystallite is slightly shorter in the [001] direction than in the [100] (or [010]) direction. To visualize differences between the obtained crystallite sizes, Table S2† lists the diameters in the [001], [100], [110] and [111] directions and Fig. 4c shows a schematic view of the crystallite shape for CWO. Despite the anisotropy being subtle, this behaviour (short along the [001] direction) is also observed in Gd^{3+}-doped phases. In contrast, the phases without Gd^{3+} present the contrary deformation exhibiting a superior size along the [001] direction than that along the [100] direction. Therefore, a particular effect in the size (apparent and anisotropic) is observed for which there is no explanation. The unique difference found for Gd^{3+} with respect to Eu^{3+} and Tb^{3+} lies in its electronic configuration since Gd^{3+} presents half-filled $4f^7$ orbitals.

Solid state photoluminescence (SSPL)

Host matrix CWO. As shown in Fig. S6,† the excitation and emission spectra of host matrix $CaWO_4$ (**CWO**) were studied. The excitation band located at 330 nm is ascribed to a charge transfer band (CTB) associated with an electron transfer from oxygen to tungsten atom in the WO_4 tetrahedral units. The corresponding blue emission is observed as a broad band with a maximum located at 470 nm.

Single-lanthanide Ln@CWO compounds. Eu@CWO exhibits an emission spectrum with peaks belonging to the transitions within the 4f shell of the Eu^{3+} ion, $^5D_0 \rightarrow {}^7F_J$ (J = 0–5), with a maximum emission at 615 nm ($^5D_0 \rightarrow {}^7F_2$), as shown in Fig. 5a. The excitation spectrum exhibits a combination of transitions with maxima at 276, 393 and 463 nm. Notably, the last lower energy transition is exceptionally deep into the visible region. In addition, the same transition $^5D_2 \leftarrow {}^7F_0$ is higher in intensity; for this reason, it was selected as the excitation wavelength (Fig. 5a). The corresponding assignment of the 4f–4f* excitation transitions for all the **Ln@CWO** compounds is displayed in Table S3.† The maximum emission

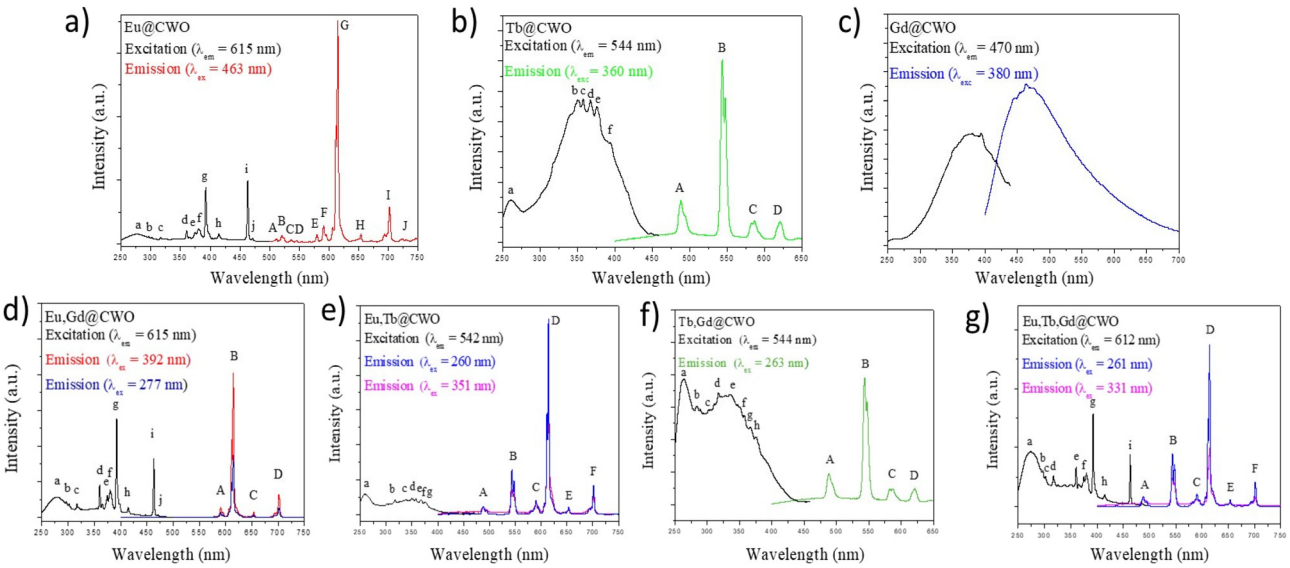

Fig. 5 (a) Excitation (λ_{em} = 615 nm) (left) and emission (λ_{ex} = 463 nm) (right) spectra of **Eu@CWO**. (b) Excitation (λ_{em} = 544 nm) (left) and emission (λ_{ex} = 360 nm) (right) spectra of **Tb@CWO**. (c) Excitation (λ_{em} = 470 nm) (left) and emission (λ_{ex} = 380 nm) (right) spectra of **Gd@CWO**. (d) Excitation (λ_{em} = 615 nm) (left) and emission (λ_{ex} = 277 nm and λ_{ex} = 393 nm) (right) spectra of **Eu,Gd@CWO**. (e) Excitation (λ_{em} = 542 nm) (left) and emission (λ_{ex} = 260 nm and λ_{ex} = 350 nm) (right) spectra of **Eu,Tb@CWO**. (f) Excitation (λ_{em} = 544 nm) (left) and emission (λ_{ex} = 263 nm) (right) spectra of **Tb,Gd@CWO**. (g) Excitation (λ_{em} = 612 nm) (left) and emission (λ_{ex} = 260 and 330 nm) (right) spectra of **Eu,Tb,Gd@CWO**.

belonging to the $^5D_0 \rightarrow {}^7F_2$ transition in **Eu@CWO** exhibits a mono-exponential decay profile with a τ_{obs} value of 1.08 ms (see Fig. S7a†). Besides, this transition is responsible for its red emission accompanied by CIE(x,y) coordinates of 0.616 and 0.377 corresponding to red emission (Fig. 6b).

The excitation spectrum of **Tb@CWO** was recorded in the 250–450 nm range, monitoring the $^5D_4 \rightarrow {}^7F_5$ emission at 544 nm (Fig. 5b). The narrow peaks labelled a–f in the excitation spectrum correspond to transitions within the 4f shell of the Tb^{3+} ion. Under direct excitation into the 4f levels ($^5G_5 \leftarrow {}^7F_6$, 360 nm), the typically narrow peaks of Tb^{3+} are observed, yielding green emission. The corresponding assignments of the excitation $^{2S+1}L_J \leftarrow {}^7F_6$ and the emission $^5D_4 \rightarrow {}^7F_6$, $^5D_4 \rightarrow {}^7F_5$, $^5D_4 \rightarrow {}^7F_4$ and $^5D_4 \rightarrow {}^7F_3$ electronic transitions are shown in Fig. 5b. The most intense emission peak located at 544 nm shows a mono-exponential decay profile (Fig. S7b†) with a τ_{obs} value of 1.05 ms. In comparison with the $Tb@CaWO_4$ nanowires obtained by Lin and colleagues, the τ_{obs} value of **Tb@CWO** increased by 28%.[43]

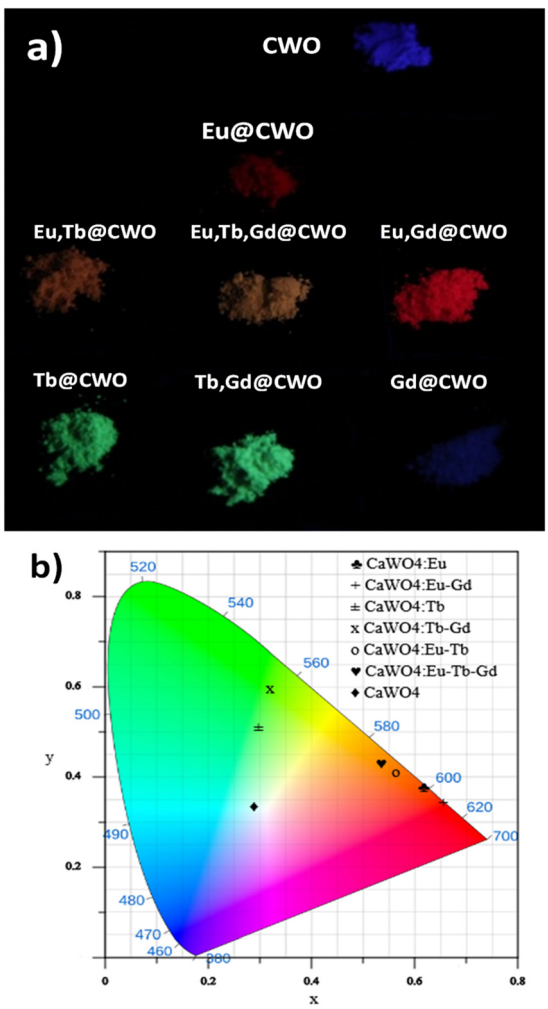

Fig. 6 (a) Powder samples under UV lamp illumination. (b) CIE diagram showing the colour performance of the studied compounds.

In the case of **Gd@CWO**, a broad band located at 470 nm is observed when the sample is excited at 380 nm (see Fig. 5c). This doped phase does not exhibit any sharp lines from the 4f shell of the Gd^{3+} ion, neither in the excitation nor in the emission spectrum. This fact is expected since the emissive level corresponding to the $^6P_{7/2}$ state of the Gd^{3+} ion lies at too high an energy level to be populated by most antenna systems.[1,6] Consequently, the excitation and emission spectra from Gd-doped samples are quite similar to those of the host matrix.

Double-lanthanide Ln,Ln′@CWO and triple-lanthanide Ln, Ln′,Ln″@CWO compounds. Co-doped samples were prepared to analyse potential energy transfer processes among emitting centres toward the improvement of luminescence properties. **Eu,Gd@CWO**, **Eu,Tb@CWO** and **Tb,Gd@CWO** were synthesized and their luminescence properties were further studied.

First, the excitation spectrum of **Eu,Gd@CWO** shows a broad band located at 277 nm accompanied by more intense peaks related to Eu^{3+} ions. From the set of peaks, the most intense is located at 393 nm and is ascribed to the $^5L_6 \leftarrow {}^7F_1$ transition. Two excitation experiments when λ_{exc} = 277 nm and 393 nm were carried out to find a feasible way to create the most intense emission spectrum. Direct lanthanide sensitization seems to be an efficient pathway to yield emission with intense peaks ascribed to the $^5D_0 \rightarrow {}^7F_J$ (J = 0–4) transitions (see Fig. 5d). Also, the excitation spectrum of **Eu,Tb@CWO** exhibited a broad band accompanied by peaks belonging to Eu^{3+} and Tb^{3+} ions, as shown in Table S3.† By excitation from the host material (260 nm), or by selecting the maximum excitation peak from the lanthanide (350 nm, $^5D_4 \leftarrow {}^7F_0$ (Eu^{3+}) transition), a typical Eu^{3+} emission is seen, which is accompanied by some peaks from Tb^{3+} ions (Fig. 5e). Due to the emissive level of Tb^{3+} (20 492 cm^{-1}) being higher than that from Eu^{3+} (17 271 cm^{-1}), it is feasibly attributed to a metal-to-metal charge transfer (MMCT) Tb → Eu, with consequent increments in the emission parameters (see Table 2). This phenomenon has been successfully explained in Tb^{3+}/Eu^{3+}@$Sc_2(WO_4)_3$ compounds.[44]

By monitoring the excitation spectrum of **Tb,Gd@CWO** at an emission centred at 544 nm, the most intense signal corresponded to the **CWO** matrix with respect to the peaks $^{2S+1}L_J \leftarrow {}^7F_6$ from Tb^{3+} ions (Fig. 5g). Then, this wavelength was selected for excitation. Upon host matrix sensitization (λ_{exc} = 263 nm), **Tb,Gd@CWO** exhibits four intense $^5D_4 \rightarrow {}^7F_n$ emission transitions (Fig. 5f and Table S3†). The most intense emission peak, $^5D_4 \rightarrow {}^7F_5$, is responsible for its green emission at 544 nm. Its mono-exponential decay profile (Fig. S7e†) shows a τ_{obs} value of 0.76 ms.

This behaviour is also reflected when the τ_{obs} values are analysed. The obtained lifetime from **Eu,Gd@CWO** is slightly smaller than that from **Eu@CWO** with values of 0.96 and 1.08 ms (see Fig. S5a and S5d†). Similarly, when τ_{obs} values of both **Tb,Gd@CWO** and **Tb@CWO** are compared, the co-doped sample exhibited a lifetime of 0.76 ms while the Tb-doped sample showed a value of 1.05 ms (see Fig. S5b and S5e†). Besides, the same effect could be seen in **Eu,Tb@CWO** in com-

Table 2 Table of luminescence parameters of the studied Eu-based materials herein

Eu-based material	I_{tot}/I_{MD}	$1/\tau_r$	τ_r/ms	k_r/s^{-1}	k_{exp}/s^{-1}	k_{nrad}/s^{-1}	τ_{obs}/ms	QY_{Eu}%
Eu@CWO	16.53	817.6	1.22	817.6	943.4	125.8	1.06	86.7
Eu,Gd@CWO	15.14	749.0	1.30	748.9	1043	293.8	0.959	71.8
Eu,Tb@CWO	14.90	737.1	1.35	737	751.9	14.83	1.33	98
Eu,Tb,Gd@CWO	13.90	687.4	1.45	687.4	900.9	213.5	1.11	76

parison with **Eu,Tb,Gd@CWO**, exhibiting a decrease of Eu^{3+} emission from 1.33 to 1.11 ms (see Fig. S5c and S5f†), but accompanied by a slight increment of τ_{obs} for Tb^{3+} from 0.52 to 0.61 ms. All these results reinforce the quencher-role of Gd^{3+} ions in the set of compounds reported herein.

From the lifetime measurements, all the decay processes were successfully fitted using a mono-exponential equation (eqn (1)):

$$I = A + I_1 \cdot e^{\frac{-t}{\tau_1}} \quad (1)$$

This model suggests the presence of one emitting centre in the structure. This behaviour can be related to the crystallographic features where each doped Ln^{3+} is edge-connected to four AO_8 polyhedra. Considering these features, the Rietveld analysis revealed that the lanthanides occupy 10% of the Ca^{2+} sites. It is possible to assume that the different lanthanide environments do not affect the emitting performance.

To qualify the ability of the host matrix to sensitize the emission of Eu^{3+} centres, and to acquire information on the relationship between the structure and photoluminescence properties, the photophysical parameters of the Eu-doped samples were analysed.

For a suitable analysis of the photoluminescence efficiency of the Eu-doped samples, the intrinsic europium quantum yield, QY_{Eu}, was calculated. This parameter expresses how well the radiative processes compete with the non-radiative pathways and indicates the optimized quantum efficiencies for these materials. Assuming that non-radiative (k_{nr}) and radiative (k_r) processes are essentially involved in the depopulation of the $^5D_0$ state, QY_{Eu} can be expressed as:

$$QY_{Eu} = k_r/(k_r + k_{nrad}) \quad (2)$$

Generally, non-radiative contributions, k_{nrad}, include back-energy transfer to the sensitizer, electron transfer quenching, lanthanide self-quenching and quenching by matrix vibrations.[45] The radiative contribution k_r can be calculated from the equation:

$$k_r = 1/\tau_r \quad (3)$$

The so-called radiative lifetime τ_{rad} can be approximated for Eu(III) using eqn (4):[46]

$$k_{rad} = (1/\tau_{rad}) = A_{MD,0} \cdot n^3 \cdot (I_{tot}/I_{MD}) \quad (4)$$

In eqn (4), $A_{MD,0}$ is the spontaneous emission probability of the $^5D_0 \rightarrow {}^7F_1$ magnetic dipole transition equal to 14.65 s^{-1}, n is the refractive index (1.5), I_{tot} is the total integrated emission of the $^5D_0 \rightarrow {}^7F_J$ (J = 0–6) transitions and I_{MD} is the integrated emission of the $^5D_0 \rightarrow {}^7F_1$ magnetic dipole transition. Besides, if τ_{rad} is known, QY_{Eu} can be calculated using the τ_{obs} value. Based on eqn (1) and (4), QY_{Eu} can be calculated as:

$$QY_{Eu} = \tau_{obs}/\tau_{rad} \quad (5)$$

At the same time, knowledge of both τ_{obs} and τ_{rad} enables the determination of the overall rate of non-radiative deactivation. Hence, the τ_{rad} value is an important parameter in the photophysical description of lanthanide luminescence. The photoluminescence parameters of **Eu@CWO**, **Eu,Gd@CWO**, **Eu,Tb@CWO** and **Eu,Tb,Gd@CWO** are summarized in Table 2.

As can be seen in Table 2, the influence of the gadolinium ions on the PL properties of doped samples disagrees with the regular performance as an enhancer of luminescence. The k_r value of **Eu@CWO**, is higher than that of the corresponding co-doped samples. Nevertheless, when Tb^{3+} is added, it promotes a decrease in the k_{nrad} value related to the energy migration mechanism from Tb → Eu (see Fig. 7). This fact is reinforced when τ_{obs} and QY_{Eu} demonstrated higher values from the set of samples (Table 2). Moreover, all the τ_{obs} values for europium reported here (Table 2) are higher than those from analogous $CaWO_4$-doped compounds, making them interesting materials for long-term red illumination applications.[32,47]

Besides, we have demonstrated the effect of a decrease of concentration quenching by incorporating Gd^{3+} as a doping ion and further improving emission of 2D-coordination polymers based on carboxylates and lanthanides (Eu and Sm).[48] Also, Kaczmarek *et al.*[49] reported the improvement in the luminescence properties in a series of co-doped $Ln@Y_2WO_6$

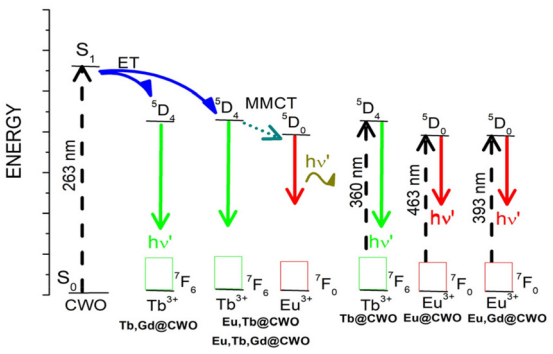

Fig. 7 Energy diagram of the Ln@CWO compounds studied herein.

(Ln: Sm, Eu, Dy) by adding Gd^{3+} ions. However, there are few investigations regarding the quenching effect by adding Gd^{3+} as a doping ion. Meza *et al.* reported quenching effects in $Eu^{3+}@Gd_2O_3$ samples, which are attributable to back energy transfer to Eu → O^{2-}.[50] Besides, Nosov *et al.* have reported the decrease in both emission intensities and lifetime values (up to 7%) of Sm^{3+} emission ($^5G_{5/2} \rightarrow {}^6H_{7/2}$) due to the incorporation of Gd^{3+} as co-dopant in a family of $NaY_{0.98-x}Sm_{0.02}Ln_xF_4$ (Ln = Gd, Lu, La) compounds.[51] The authors explain this fact in terms of a distortion in the local geometry of the emissive ions due to the presence of Gd^{3+}, yielding an increase in k_{nrad}. Moreover, high-quality light performance requires obtaining the Commission International de l'Eclairage (CIE) *x*,*y* coordinates, with correlated colour temperature (CCT) parameters for lighting applications. The quantification of colour emission of different luminescent materials allows their comparison by studying the corresponding light-emitting performance. In this sense, the colour coordinates are usually calculated using the CIE *x*,*y* chromaticity system and plotted in a two-dimensional diagram. The colour emission of all the compounds was quantified as displayed in Fig. 6. Also, all the samples showed CCT values between 1800 and 7800 K, respectively (see Table 3), matching the human eye-friendly application range.

Table 3 CIE *x*,*y* coordinates, colour emission and correlated colour temperatures of the studied compounds

Material	CIE *x*	CIE *y*	Colour	CCT (K)
Eu@CWO	0.616	0.377	Reddish orange	1836.4
Tb@CWO	0.298	0.51	Yellowish green	6271.9
Eu,Tb@CWO	0.565	0.409	Orange	1782.3
Eu,Gd@CWO	0.656	0.343	Reddish orange	2854.1
Tb,Gd@CWO	0.321	0.591	Yellowish green	5703
Eu,Tb,Gd@CWO	0.535	0.429	Yellowish orange	2049.5
CWO	0.289	0.334	Blue	7833.2

Finally, as a "proof of concept" for the design and fabrication of devices, **Eu@CWO**, **Eu,Gd@CWO**, **Eu,Tb@CWO** and **Eu,Tb,Gd@CWO** were selected and deposited onto glass substrates using a spin-coating technique.

Spin coating is a thin-film coating technique using a flat substrate (*e.g.* gold, copper, glass) applying a film with thickness at the nano- or microscale. The functional thin films are coated on glass or single-crystal substrates. To fabricate oxide layers, the precursors are usually prepared through the "sol–gel" route, and after spin coating, the substrates are heated at high temperature to obtain the oxide layer.[52] Homogeneity and uniformity are critical properties of thin films for device implementations for technological applications that require a reproducible and confident response, such as photocatalysis, sensing and visible light emitters.[53]

After several experiments, the most optimal variables for film design with these materials were 2000 rpm, 1 min per step, with a volume of 0.25 mL of 20 mg mL^{-1} concentration added onto the glass substrate, resulting in films with the best homogeneity and coverage.

As can be seen in Fig. 8, homogeneously uniform and flat films are obtained with a measured cross-section of 147 μm. A retro-dispersed electron micrograph (Fig. 8f) can also give information regarding the uniformity and the absence of surface defects. Besides, under UV illumination, the films conserve luminescence as if in powder form (see insets in Fig. 9), which is desirable for exploring potential sensing applications for small molecules.

Finally in order to analyse the red-emission performance of Eu-based films, steady-state luminescence measurements were

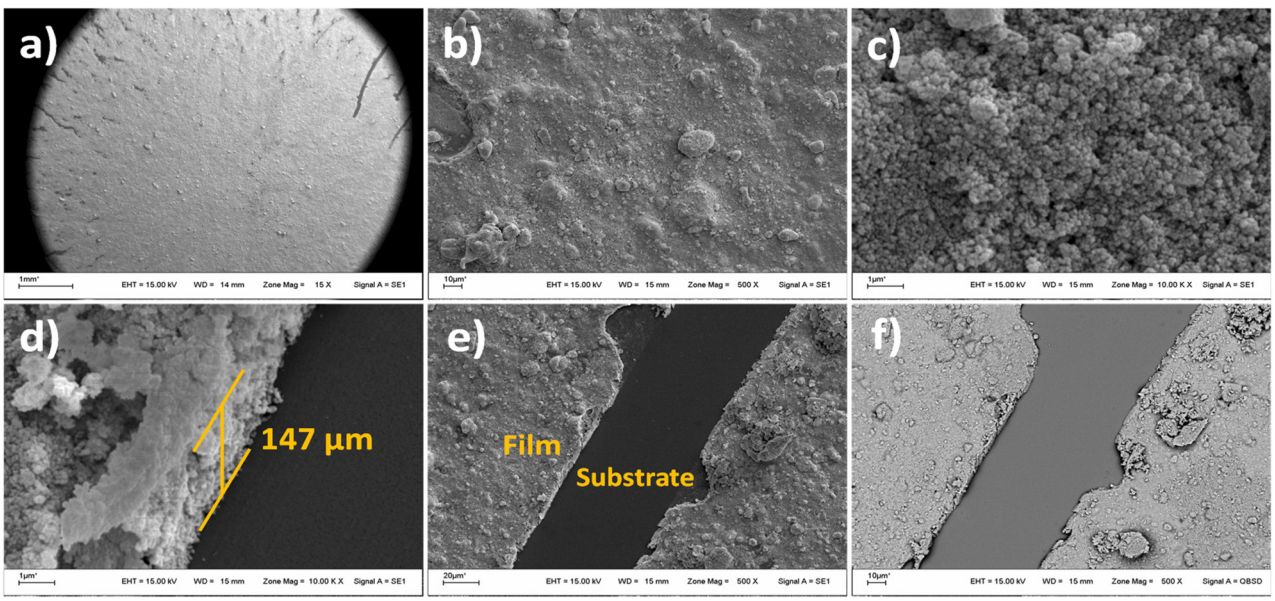

Fig. 8 SEM images of film I observed at 15× (a), 500× (b) and 1000× (c and d) magnification. (e) Micrograph of the thin film observed at 500× magnification. (f) Retro-dispersed electron image.

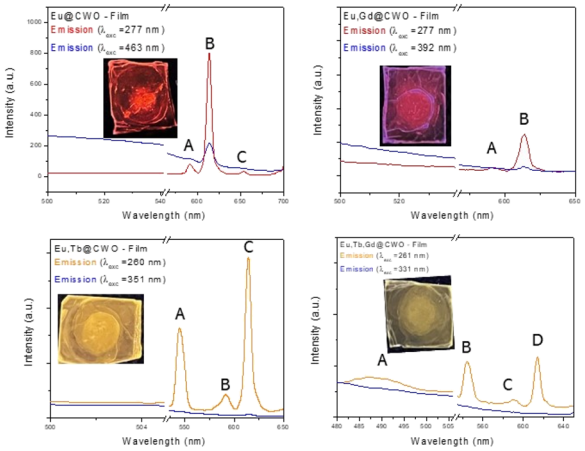

Fig. 9 PL spectra of the films upon excitation with light of two different wavelengths and photographs (insets) of the thin films upon UV irradiation.

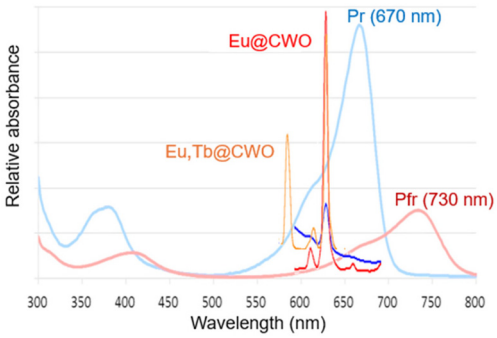

Fig. 10 PL emission spectra of **Eu@CWO** and **Eu,Tb@CWO** in addition to the absorption of biologically active states P_r and P_{fr} in plants.

performed. As can be seen in Fig. 9, there is a particular sensitization of lanthanide emission, through matrix excitation. A direct lanthanide excitation seems not the best choice to enhance the radiative pathways as the intensities in the emission spectra are relatively much lower. The absorption of the biologically active states P_{fr} and P_r in plants is also shown in Fig. 10 for comparison with the $^5D_0 \rightarrow {}^7F_2$ transition signal. A significant overlap can be found, indicating that Eu^{3+} emission in both powder or thin films can be utilized as light for plant growth.

Conclusions

A set of phases with formula $Ca_{1-2x}Ln_xNa_xWO_4$ (x = 0 and 0.1; Ln = Eu, Tb and Gd) (namely **Eu@CWO**, **Tb@CWO** and **Gd@CWO**) and co-doped phases with $Ln_xLn'_y$ = $Eu_{0.05}Tb_{0.05}$, $Eu_{0.05}Gd_{0.05}$, $Tb_{0.05}Gd_{0.05}$ (**Eu,Tb@CWO**, **Eu,Gd@CWO** and **Tb, Gd@CWO**) and $Eu_{0.033}Tb_{0.033}Gd_{0.033}$ (**Eu,Tb,Gd@CWO**) was successfully synthesized using a sol–gel method followed by calcination at mild temperatures yielding micro-structures of around 10–200 μm. Besides, an in-depth structural and microstructural analysis was carried out by employing powder X-ray diffraction accompanied by Rietveld refinements. This study is remarkable for its novelty in covering wolframate-type compounds that are not commonly reported, which is important for designing micro- and nanomaterials. Moreover, the solid-state photoluminescence (SSPL) in the visible region was analysed by recording the excitation and emission spectra and calculating the lifetimes from the decay profiles. Besides, the intrinsic europium quantum yields (QYs), radiative and non-radiative constants and CIE colour coordinates were calculated and related to the energy transfer processes between lanthanides and the host matrix. The QYs fall into the 76–98% range with the highest value obtained being that for the **Eu, Tb@CWO** sample. This result demonstrates an efficient energy transfer from Tb^{3+} to Eu^{3+} to yield visible photoluminescence accompanied by the longest τ_{obs} value in the set (1.33 μs). Finally, the europium-based compound was selected for thin-film fabrication by an immobilizing spin-coating method and by controlling several experimental parameters, a homogeneous thin-film coating with ross-section of 150 μm on a glass substrate was yielded. These results indicate that Eu-containing CWO materials have potential for application in indoor plant cultivation LED devices and solid-state visible-light emitters with variety in their colour of luminescence.

Data availability

The data supporting this article have been included as part of the ESI.†

Conflicts of interest

There are no conflicts to declare.

Acknowledgements

This work was supported by the Consejo Nacional de Investigaciones Científicas y Técnicas (CONICET), AGENCIA and Universidad Nacional de San Luis (projects: PIP 2972, PICT 20202-2437 and PROICO 02-2320). V. P. thanks the Ph.D. CONICET fellowship for the financial support. G. E. G., C. A. L. and G. E. N. are members of CIC-CONICET (Carrera del Investigador Científico). We also thank Lic. Esteban Crespo from INFAP-UNSL for his assistance in SEM measurements.

References

1 N. Yeh and J. Chung, *Renewable Sustainable Energy Rev.*, 2009, **13**, 2175–2180.
2 M. Olle and A. Viršile, *Agric. Food Sci.*, 2013, **22**, 223–234.
3 K. Li and R. Van Den, *Chem. Commun.*, 2019, **55**, 10697–10700.

4 W. Kang, J. Park, K. Park and J. Son, *Hortic., Environ. Biotechnol.*, 2016, **57**, 573–579.
5 M. Sabzalian, P. Heydarizadeh, M. Zahedi, A. Boroomand, M. Agharokh, M. Sahba and B. Schoefs, *Agron. Sustainable Dev.*, 2014, **34**, 879–886.
6 Y. Tsai, C. Chiang, W. Zhou, J. Lee, H. Sheu and R. Liu, *J. Am. Chem. Soc.*, 2015, **137**, 8936–8939.
7 C.-T. Chen, T.-J. Lin, M. S. Molokeev and W.-R. Liu, *Dyes Pigm.*, 2018, **150**, 121–129.
8 K. Li, M. Shang, H. Lian and J. Lin, *J. Mater. Chem. C*, 2016, **4**, 5507–5530.
9 T. Pulli, T. Dönsberg, T. Poikonen, F. Manoocheri, P. Kärhä and E. Ikonen, *Light: Sci. Appl.*, 2015, **4**, 332.
10 Z. Zhou, J. Zheng, R. Shi, N. Zhang, J. Chen, R. Zhang, H. Suo, E. Goldys and C. Guo, *ACS Appl. Mater. Interfaces*, 2017, **9**, 6177–6185.
11 G. D. Massa, H. Kim, R. M. Wheeler and C. A. Mitchell, *HortScience*, 2008, **43**, 1951–1956.
12 H. Yu, J. Chan, B. Devakumar and X. Huang, *Mater. Today Chem.*, 2023, **30**, 101548.
13 N. Ma, W. Li, B. Devakumar, Z. Zhang and X. Huang, *Mater. Today Chem.*, 2021, **21**, 100512.
14 K. Binnemans, *Chem. Rev.*, 2009, **109**, 4283–4374.
15 C. D. S. Brites, P. P. Lima, N. J. O. Silva, A. Millán, V. S. Amaral, F. Palacio and L. D. Carlos, *New J. Chem.*, 2011, **35**, 1177.
16 L. D. Carlos, R. A. S. Ferreira, V. de Z. Bermudez and S. J. L. Ribeiro, *Adv. Mater.*, 2009, **21**, 509–534.
17 J.-C. G. Bünzli, S. Comby, A.-S. Chauvin and C. D. B. Vandevyver, *J. Rare Earths*, 2007, **25**, 257–274.
18 N. Ma, W. Li, B. Devakumar and X. Huang, *Inorg. Chem.*, 2022, **61**, 6898–6909.
19 X. Huang, J. Liang, S. Rtimi, B. Devakumar and Z. Zhang, *Chem. Eng. J.*, 2021, **405**, 126950.
20 S. Wang, Q. Sun, B. Devakumar, J. Liang, L. Sun and X. Huang, *J. Alloys Compd.*, 2019, **804**, 93–99.
21 E. G. Moore, A. P. S. Samuel and K. N. Raymond, *Acc. Chem. Res.*, 2009, **42**, 542–552.
22 J.-C. G. Bünzli, *Chem. Rev.*, 2010, **110**, 2729–2755.
23 K. Zhenga and P. Ma, *Dalton Trans.*, 2024, **53**, 3949–3958.
24 G. Xiang, Z. Liu, Z. Yang, Y. Wang, L. Yao, S. Jiang, X. Zhou, L. Li, X. Wang and J. Zhang, *J. Mater. Chem. C*, 2023, **11**, 16310–16315.
25 D. Yue, Q. Li, W. Lu, Q. Wang, M. Wang, C. Li, L. Jin, Y. Shi, Z. Wang and J. Hao, *J. Mater. Chem. C*, 2015, **3**, 2865–2871.
26 M. Lin, L. Xie, Z. Wang, B. S. Richards, G. Gao and J. Zhong, *J. Mater. Chem. C*, 2019, **7**, 2971–2977.
27 W. Bai, Y. Liu, Y. Wang, X. Qiang and L. Feng, *Ceram. Int.*, 2015, **10**, 12896–12900.
28 (*a*) R. Saraf, C. Shivakumara, N. Dhananjaya, S. Behera and H. Nagabhushana, *J. Mater. Sci.*, 2015, **50**, 287–298; (*b*) R. Z. Zhuang, L. Z. Zhang, Z. B. Lin and G. F. Wang, *Mater. Res. Innovations*, 2008, **12**, 62–65; (*c*) S. Belogurov, V. Kornoukhov, A. Annenkov, A. Borisevich, *et al.*, *IEEE Trans. Nucl. Sci.*, 2015, **52**, 1131–1135; (*d*) Z. Hou, R. Chai, M. Zhang, C. Zhang, P. Chong, Z. Xu, G. Li and J. Lin, *Langmuir*, 2009, **25**, 12340–12348.
29 J. Liu, A. M. Kaczmarek, J. Billet, I. Van Driessche and R. Van Deun, *Dalton Trans.*, 2016, **45**, 12094–12102.
30 J. Huang, Q. Li, J. Wang, L. Jin, B. Tian, C. Li, Y. Shi, Z. Wang and J. Hao, *Dalton Trans.*, 2018, **47**, 8611–8618.
31 (*a*) Y. Xie, S. Ma, Y. Wang, M. Xu, C. Lu, L. Xiao and S. Deng, *Opt. Mater.*, 2018, **77**, 13–18; (*b*) R. Saraf, C. Shivakumara, N. Dhananjaya, S. Behera and H. Nagabhushana, *J. Mater. Sci.*, 2015, **50**, 287–298; (*c*) A. Xie, X. Yuan, S. Hai, J. Wang, F. Wang and L. Li, *J. Phys. D: Appl. Phys.*, 2009, **42**, 105107; (*d*) A. Khanna and P. S. Dutta, *J. Solid State Chem.*, 2013, **198**, 93–100; (*e*) Z. H. Zhang, Q. Huang, X. Zhao and Z. L. Huang, *Phys. Status Solidi*, 2009, 2839–2843; (*f*) J. Zhang, L. Li, W. Zi, N. Guo, L. Zou, S. Gan and G. Ji, *J. Phys. Chem. Solids*, 2014, **75**, 878–887; (*g*) C. Du, F. Lang, Y. Su and Z. Liu, *J. Colloid Interface Sci.*, 2013, **394**, 94–99; (*h*) Z. Zhou, Y. Yu, X. Liu, W. Ye, G. Hu, B. Lei and Y. Yan, *J. Adv. Ceram.*, 2015, **4**, 318–325.
32 G. E. Gomez, C. A. López, R. L. Ayscue III, K. E. Knope, M. del R. Torres Deluigi and G. E. Narda, *Dalton Trans.*, 2019, **48**, 12080–12087.
33 L. Yun, W. Shi-yu, L. Jin-yang and S. Xiao-lei, *Chin. J. Lumin.*, 2014, **35**, 1201–1204.
34 Y. Ouyang, X. Zhang, J. Wang, X. Wang and X. He, *Cailiao Daobao*, 2016, **30**, 33–37.
35 H. M. Noh, E. O. Kim, J. H. Jeong, K. R. Kang, Y. J. Kim, K. C. Lee, J. H. Lee, Y. D. Park and J. H. Kim, *New Phys.: Sae Mulli*, 2014, **64**, 717–722.
36 C. Li, C. Lin, X. Liu and J. Lin, *J. Nanosci. Nanotechnol.*, 2008, **8**, 1183–1190.
37 D. Athayde, D. F. Souza, A. Silva, D. Vasconcelos, E. H. Nunes, J. C. D. da Costa and W. Vasconcelos, *Ceram. Int.*, 2016, **42**, 6555–6571.
38 H. M. Rietveld, *J. Appl. Crystallogr.*, 1969, **2**, 65–71.
39 J. Rodríguez-Carvajal, *Phys. B*, 1993, **192**, 55–69.
40 P. Thompson, D. E. Cox and J. B. Hastings, *J. Appl. Crystallogr.*, 1987, **20**, 79–83.
41 R. M. Hazen, L. W. Finger and J. W. E. Mariathasan, *J. Phys. Chem. Solids*, 1985, **46**, 253–263.
42 R. D. Shannon, *Acta Crystallogr., Sect. A*, 1976, **32**, 751–767.
43 Z. Hou, C. Li, J. Yang, H. Lian, P. Yang, R. Chai, Z. Cheng and J. Lin, *J. Mater. Chem.*, 2009, **19**, 2737.
44 B. Fu, H. Yan, R. Li, Z. Liao, B. Qiu, G. Gong, H. Huang, Y. Sun, H. Wen and J. Liao, *Dalton Trans.*, 2024, **53**, 798–807.
45 A. Beeby, I. M. Clarkson, R. S. Dickins, S. Faulkner, D. Parker, L. Royle, A. S. de Sousa, J. A. G. Williams and M. Woods, *J. Chem. Soc., Perkin Trans. 2*, 1999, 493–504.
46 A. Chauvin, F. Gumy, D. Imbert and J. G. Bünzli, *Spectrosc. Lett.*, 2004, **37**(5), 517–532.
47 S. Bai, Y. Liu, G. Tan, W. Liu, D. Liu, R. Wang, Y. Zhu, S. Ye and H. Ren, *J. Lumin.*, 2020, **225**, 117351.
48 G. E. Gomez, M. C. Bernini, E. V. Brusau, G. E. Narda, D. Vega, A. M. Kaczmarek, R. Van Deun and M. Nazzarro, *Dalton Trans.*, 2015, **44**, 3417–3429.

49 A. M. Kaczmarek, K. V. Hecke and R. Van Deun, *Inorg. Chem.*, 2014, **53**, 9498–9508.
50 O. Meza, E. G. V. Leal, L. A. Diaz-Torres, H. Desirena, J. L. Rodríguez-López and E. Pérez, *J. Phys. Chem.*, 2014, **118**(8), 1390–1396.
51 V. G. Nosov, A. A. Betina, T. S. Bulatova, P. B. Guseva, I. E. Kolesnikov, S. N. Orlov, M. S. Panov, M. N. Ryazantsev, N. A. Bogachev and M. Y. Skripkin, *Materials*, 2023, **16**, 2157.
52 G. George, S. R. Ede and Z. Luo, *Fundamentals of Perovskite Oxides: Synthesis, Structure, Properties and Applications*, 1st edn, 2020.
53 S. Majumder, *Nanostructured Materials for Visible Light Photocatalysis*, Elsevier, 2022, pp. 47–113.